

Protein Kinase A and assembly of an ABCC4 protein network

Received: 22 January 2024

Accepted: 18 November 2025

Published online: 03 December 2025

 Check for updates

Jingwen Zhu^{1,7}, Sabina Ranjit^{1,7}, Tomoka Gose¹, Amanda Nourse², Vishwajeeth R. Pagala³, Zuo-Fei Yuan³, John Lynch¹, Yao Wang¹, Aaron Pitre^{1,4}, Rebecca Crawford¹, Junmin Peng^{2,5}, Juwina Wijaya¹, Anjaparavanda P. Naren⁶ & John D. Schuetz¹✉

Cyclic AMP (cAMP) compartmentalization at the plasma membrane employs export by ABCC4, yet the protein machinery that creates spatially restricted signaling has remained unclear. We show that robust PKA activation increases ABCC4 at the cell surface and assembles a PDZ-dependent macromolecular complex that constrains ABCC4 mobility and stabilizes the transporter. Using Avi-tag crosslinking/AP-MS and APEX proximity labeling, we map a PKA-induced ABCC4 neighborhood enriched for PDZ-domain scaffolds that couple ABCC4 to actin and cell junctions. SCRIB emerges as a previously unrecognized interactor whose depletion lowers surface ABCC4 and blunts ABCC4-dependent drug resistance. Deleting the ABCC4 PDZ motif accelerates lateral diffusion ~4-fold, halves protein half-life, and attenuates PKA-stimulated increases in surface ABCC4 and cAMP efflux, establishing a requirement for the PDZ motif in optimal export under PKA drive. Finally, the selective ABCC4 inhibitor Ceefourin-2 lowers ABCC4's melting temperature and dismantles the actin/junction-enriched neighborhood, revealing a non-classical small molecule inhibitory mechanism based on network disruption. These findings define a PKA-driven, PDZ-dependent ABCC4 protein neighborhood that stabilizes the transporter and optimizes cAMP efflux—an advance over prior work that localized ABCC4 but lacked a mechanistic blueprint for its membrane microdomain organization.

Cyclic adenosine monophosphate (cAMP), a ubiquitous second messenger, is synthesized by adenylyl cyclase and affects an array of cellular processes after engaging a downstream effector like Protein Kinase A (PKA)¹. After formation, cAMP rapidly diffuses in cells ($130\text{--}700\ \mu\text{m}^2\ \text{s}^{-1}$), and depending on its concentration, can cause either broad cellular or more locally restricted PKA activation^{2,3}. Establishment of cAMP concentration gradients in membranes, by membrane export of cAMP, is termed compartmentalization (or microdomains),

and these have been empirically demonstrated by using genetically encoded sensors based on PKA and EPAC (exchange protein directly activated by cAMP)^{4,5}. We and others have shown that the compartmentalization of cAMP is readily revealed after PKA activation by the diterpene activator of adenylyl cyclase, forskolin^{6–8}, which activates most cellular adenylyl cyclases⁹. Knowledge of the protein machinery executing the formation of cAMP microdomains by ATP-binding cassette (ABC) transporters such as ABCC4^{6,8,10–12} is unknown.

¹Department of Pharmacy and Pharmaceutical Sciences, St. Jude Children's Research Hospital, Memphis, TN, USA. ²Department of Structural Biology, St. Jude Children's Research Hospital, Memphis, TN, USA. ³Center for Proteomics and Metabolomics, St. Jude Children's Research Hospital, Memphis, TN, USA. ⁴Cell and Tissue Imaging Center, St. Jude Children's Research Hospital, Memphis, TN, USA. ⁵Department of Developmental Neurobiology, St. Jude Children's Research Hospital, Memphis, TN, USA. ⁶Department of Medicine, Cedars-Sinai Medical Center, Los Angeles, CA, USA. ⁷These authors contributed equally: Jingwen Zhu, Sabina Ranjit. ✉ e-mail: john.schuetz@stjude.org

ABCC4, an ABC transporter that has been localized to caveolae with established roles in cAMP signaling^{13–15}, can carry out cAMP compartmentalization, especially after PKA activation^{6,16}. ABCC4 has a highly conserved C-terminal PDZ motif: glutamate–threonine–alanine–leucine (ETAL). However, it is unknown if PKA activation drives ABCC4 to the plasma membrane, or if protein interactions mediated this, and is the ABCC4 PDZ motif required for this process.

Here, we demonstrate that strong PKA activation promotes ABCC4 plasma membrane localization, which is associated with the formation of an extensive protein network. Our studies identify key components of this protein network and show that the ABCC4 PDZ motif confines ABCC4 movement in the plasma membrane (and is not essential for plasma membrane localization), likely by enabling the PKA-dependent formation of a “neighborhood” protein complex that connects ABCC4 to the actin cytoskeleton network. We also demonstrated that this network is disrupted by a potent specific ABCC4 inhibitor, which suggests a previously uncharacterized mechanistic basis for how some ABCC4 inhibitors function.

Results

The PDZ motif of ABCC4 restrains ABCC4 movement at the plasma membrane

To investigate the effect of a conserved 4 amino acid type II PDZ motif on ABCC4, we deleted the PDZ motif (Δ PDZ) from a construct expressing either GFP-tagged ABCC4 or that expressing Avi-tagged ABCC4 (see details about this plasmid in later sections) by inducing an early stop codon upstream of the PDZ motif coding sequence. These constructs were then introduced into the HEK293 ABCC4-KO cells (see characterization of HEK293 ABCC4-KO cells in Supplementary Fig. 1) to study the effect of the PDZ motif. We first determined if ABCC4 localization at the plasma membrane was altered by the absence of the PDZ motif. ABCC4-KO cells transiently expressing GFP-ABCC4 or GFP-ABCC4 Δ PDZ were labeled with Sulfo-succinimidyl 2-(biotinamido)ethyl-1,3'-dithiopropionate (Sulfo-NHS-SS-Biotin), a cell membrane impermeable reagent that biotinylates proteins protruding from the cell surface (Supplementary Fig. 3a). This study found that ABCC4 lacking PDZ (Δ PDZ) motif exhibits minor alteration in translocation efficiency to the plasma membrane (Supplementary Fig. 3a). Similarly, iodixanol density fractionation in cells stably expressing Avi-ABCC4 or Avi-ABCC4 Δ PDZ suggested both variants substantially distributed in the plasma membrane fractions where Na⁺ K⁺ ATPase (ATP1A1) serving as a marker (Supplementary Fig. 2c and d). To complement these findings, we conducted fluorescence confocal microscopy. GFP-ABCC4 Δ PDZ exhibited slightly lower overall fluorescence compared to full-length (FL) ABCC4. Interestingly, at low to moderate expression levels, GFP-ABCC4 Δ PDZ distinctly colocalized with the plasma membrane marker Wheat Germ Agglutinin conjugated with Alexa Fluor 647 (WGA-647) almost identically to GFP-ABCC4 (Supplementary Fig. 3b). However, at high expression levels, GFP-ABCC4 Δ PDZ displayed a more diffuse distribution than ABCC4 (Supplementary Fig. 3b). This observation prompted us to study the impact of the PDZ motif on the movement and stability of ABCC4.

Using total internal reflection fluorescence microscopy (TIRF) and single-particle tracking, we traced the movement trajectory of GFP-ABCC4 or GFP-ABCC4 Δ PDZ. Cells expressing ABCC4 showed little detectable movement (Fig. 1a left panel, Supplementary Movie 1), whereas GFP-ABCC4 Δ PDZ rapidly moved at nearly 4 times the rate of GFP-ABCC4 FL (Fig. 1a middle and right panels, Supplementary Movie 2). The stability of ABCC4 variants was investigated using a cycloheximide (CHX) chase assay. Exogenous ABCC4 variants (i.e., Avi-ABCC4 and Avi-ABCC4 Δ PDZ) are less stable compared to endogenous ABCC4 (Supplementary Fig. 2b). But it is more striking that deletion of the PDZ domain reduced the half-life of ABCC4 by about 2-fold (Fig. 1b), suggesting that the PDZ motif enhances ABCC4 stability.

Increased intracellular cAMP promotes ABCC4-mediated transport

Forskolin (FSK), a diterpene that directly activates adenylate cyclase to stimulate cAMP synthesis, and isobutyl methylxanthine (IBMX), a non-specific phosphodiesterase inhibitor, were used to promote a global increase in intracellular cAMP accumulation in HEK293 cells^{17,18}. Following FSK and IBMX treatment, extracellular cAMP levels increased markedly but were significantly reduced by Ceefourin 2 (Cee2), a potent and specific ABCC4 inhibitor¹⁹ (Fig. 1c). We next evaluated whether isoproterenol, which increases cellular cAMP by stimulating β 1-adrenergic receptors (β 1-ARs), a relatively less effective pathway, could increase extracellular cAMP²⁰. Isoproterenol induced only a modest increase in extracellular cAMP (Supplementary Fig. 11a). Cee2 reduced cAMP export regardless of the mechanism of cAMP increase.

PDZ motif absence attenuates PKA-induced increase in plasma membrane ABCC4 expression

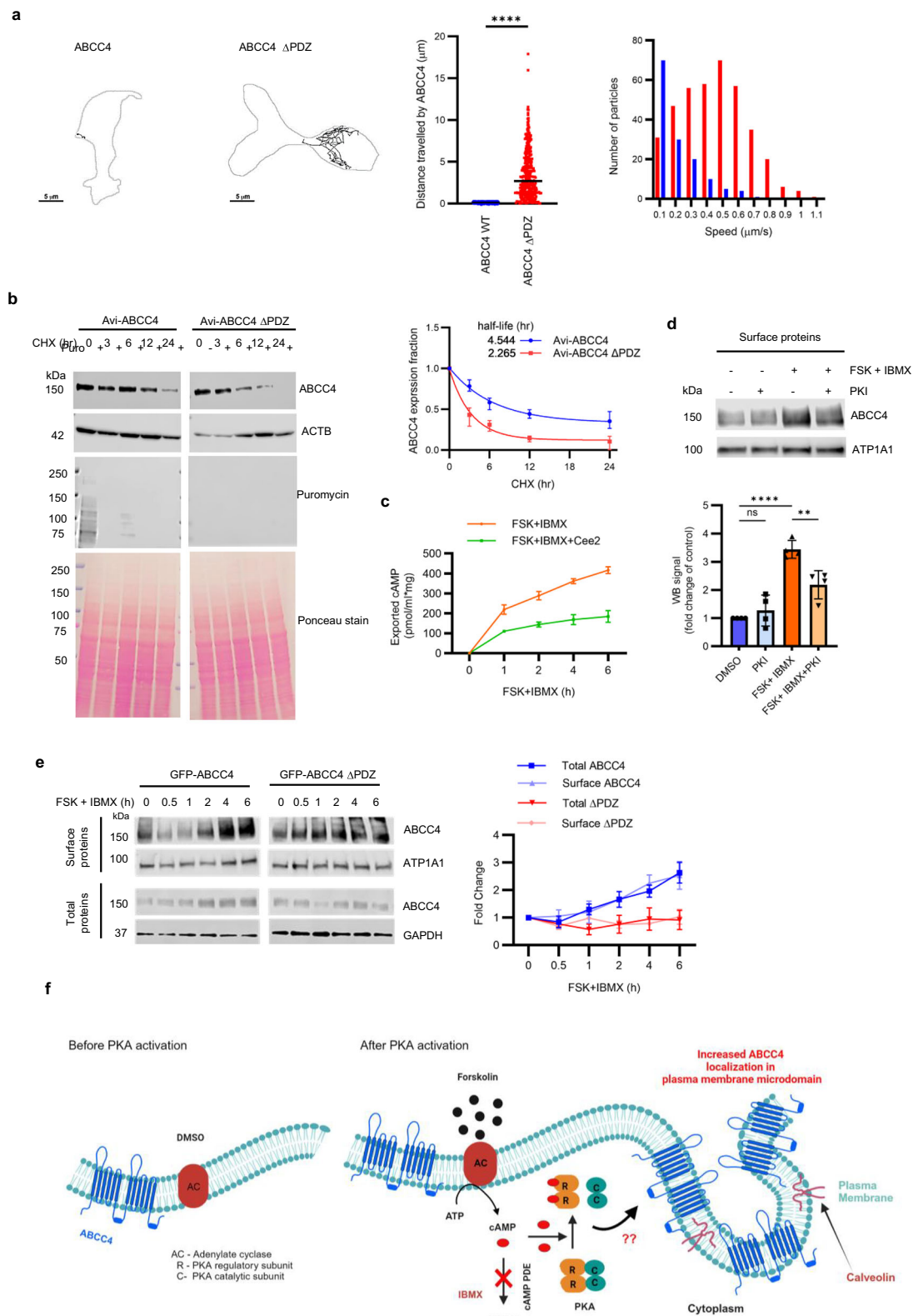
To determine whether activated cAMP-PKA signaling promoted ABCC4 function by affecting ABCC4 expression at the plasma membrane, we treated the GFP-ABCC4 transiently transfected cells with FSK and IBMX with or without the specific PKA inhibitor peptide PKI-14–22 (PKI). Surface proteins were labeled with Sulfo-NHS-SS-Biotin and precipitated by streptavidin beads (Fig. 1d). FSK and IBMX treatment increased the amount of ABCC4 at the plasma membrane, which was significantly reduced by the PKA inhibitor. This result confirmed that PKA activation elevated ABCC4 level at the plasma membrane (Fig. 1d). The lack of change in ATP1A1 with either treatment suggests the effect is specific to ABCC4. Of note, by exploiting a surface labeling approach in cells transiently expressing GFP-ABCC4 treated with FSK and IBMX for various intervals between 0 and 6 h, we discovered that PKA activation increased this exogenous ABCC4 expression at the plasma membrane by upregulating its total expression (Fig. 1e, GFP-ABCC4). Confocal microscopy live-cell imaging also shows increased total GFP-ABCC4 membrane levels after PKA activation (Supplementary Fig. 4a and b). Although the total level of endogenous ABCC4 in HEK293 was not increased by PKA hyperactivation (Supplementary Fig. 4c, input), a larger proportion of ABCC4 was localized to the plasma membrane after PKA activation (Supplementary Fig. 4c and d). This observation matched our iodixanol density gradient fractionation results, which revealed that PKA activation subtly shifted ABCC4 towards the plasma membrane fractions (Supplementary Fig. 2e). These findings show that PKA signaling promoted the plasma membrane localization of either transiently or stably expressed ABCC4.

Treatment with FSK and IBMX for up to 6 hours did not alter the membrane surface levels of GFP-ABCC4 Δ PDZ, suggesting that the PDZ motif is required for ABCC4's response to PKA activation (Fig. 1e).

PDZ motif is required for ABCC4 optimal transport of cAMP

Based on the striking lack of plasma membrane localization of ABCC4 containing the PDZ motif compared to the Δ PDZ variant, we hypothesized that unique proteins interact with ABCC4 through its PDZ motif and may be required for its stable expression at the plasma membrane. To identify ABCC4 PDZ motif-interacting proteins, we expressed ABCC4 with or without the PDZ motif in the Avi-tag system. These constructs harbor both an in-frame Avi-tag—a 15-amino acid peptide recognized and biotinylated by biotin ligase—on the N-terminus and an open reading frame encoding biotin ligase (Fig. 2a)²¹. Either Avi-ABCC4 or Avi-ABCC4 Δ PDZ was stably introduced into HEK293 ABCC4-KO cells (Fig. 2a). A cell population expressing Avi-ABCC4 at a level comparable to the endogenous ABCC4 in WT was selected (Supplementary Fig. 2a right panel).

We assessed the function of Avi-ABCC4 and Avi-ABCC4 Δ PDZ by treating their expressing cells with two cytotoxic ABCC4 drug substrates: bis-POM-PMEA or irinotecan (Supplementary Fig. 2f, left and



middle panels). Both Avi-ABCC4 and Avi-ABCC4 Δ PDZ cells exhibited higher and comparable survival rates vs. the HEK293 *ABCC4*-KO cells, thus demonstrating that both *ABCC4* expression constructs promoted survival and were functional. Both cell lines were equivalently sensitive to mitoxantrone, a control, which indicated that these cells were not generally resistant to all cytotoxins (Supplementary Fig. 2f right panel). Their functions in bis-POM-PMEA transport were not affected by PKA activation (Supplementary

Fig. 2g). Next, we quantified the extracellular cAMP level in the cultured media of Avi-ABCC4 or Avi-ABCC4 Δ PDZ cells before and after PKA activation. Extracellular cAMP levels before PKA activation were undetectable, which might be due to the low sensitivity of the assay. After PKA activation, the amount of cAMP efflux from Avi-ABCC4 cells was significantly higher than Avi-ABCC4 Δ PDZ cells, suggesting that the PDZ motif is required for maximal efflux of cAMP by *ABCC4* (Fig. 2b).

Fig. 1 | Deleting the PDZ motif causes rapid movement of ABCC4 and prevents PKA-induced increase in ABCC4 expression. **a** Fluorescent particles of GFP-ABCC4 or GFP-ABCC4 Δ PDZ were analyzed using TIRF microscopy. Plasma membrane trajectory (left panel, scale bar = 5 μ m), travel distance (middle panel), and movement speed (right panel) of ABCC4 with or without the PDZ motif. The travel distances of 277 ABCC4 particles and 385 ABCC4 Δ PDZ particles were analyzed. **** $P < 0.0001$, unpaired two-tailed Student's t test. **b** HEK293 ABCC4-KO cells stably expressing Avi-ABCC4 or Avi-ABCC4 Δ PDZ were treated with cycloheximide (for the indicated intervals to estimate ABCC4 turnover. Puromycin was added 10 min before the endpoint to evaluate the CHX effect on blocking nascent protein synthesis. Representative immunoblots from 3 independent experiments are shown on the left. Half-lives of ABCC4 variants were assessed by densitometric quantification of ABCC4 expression normalized to ACTB and are shown as mean \pm SEM in the graph on the right. **c** HEK293 WT cells were treated with Cee-fourin 2 (Cee2, 20 μ M) or DMSO for 48 h followed by FSK (50 μ M) and IBMX

(100 μ M) treatment for 0–6 h. Mean \pm SEM of extracellular cAMP levels from 3 independent experiments is shown. **d** HEK293 ABCC4-KO cells transiently transfected with ABCC4 were treated with PKI-14-22 (PKI, 8 μ M) overnight, followed by either DMSO or (FSK + IBMX) for 4 h on the next day. Representative immunoblots from 4 independent experiments are shown on the upper panel. Bars (mean \pm SD) in the bottom panel represent ABCC4 surface expression normalized to plasma membrane marker ATP1A1. **** $P < 0.0001$, ** $P < 0.01$ (p -value = 0.0026), ns non-significance; one-way ANOVA. **e** HEK293 ABCC4-KO cells transiently expressing GFP-ABCC4 or GFP-ABCC4 Δ PDZ with the indicated treatment were subjected to surface labeling analysis. Representative immunoblots (left) and densitometric quantification (right) of total and surface ABCC4 variants from 3 independent experiments are shown. Bars are mean \pm SEM. **f** The possible role of (FSK + IBMX)-induced PKA activation in modulating ABCC4 localization. Figure was created in BioRender. Ranjit, S. (2025) <https://BioRender.com/rmtl1xe>.

PKA activation and ABCC4 protein complex formation

Figure 2a depicts the scheme to detect enrichment of ABCC4 interacting proteins using the Avi-tag strategy. To enhance capture of most protein interactors, including transient ABCC4 interactions, we used the water-insoluble cross-linker dithiobis (succinimidyl propionate) (DSP). DSP features an NHS ester that reacts with primary amines in the proteins to form stable amide bonds²². Affinity purification with mass spectrometry (AP-MS) was used as an unbiased approach to interrogate proteins interacting with both Avi-ABCC4 and Avi-ABCC4 Δ PDZ. Significance analysis of Interactome (SAINT) was used to identify the statistically significant interactors of ABCC4²³. 37 proteins had significant enrichment (SAINT score >0.9 , false discovery rate (FDR) $< 5\%$) by Avi-ABCC4 after PKA activation; however, their interactions required the presence of the PDZ motif depicted in the heat map (Fig. 2c, Supplementary Table 1). SCRIB was identified as the most significant ABCC4 interactor both before and after PKA activation (Supplementary Table 1). Pathway analysis using Enrichr (GO Cellular Component 2025) illustrated enrichment of proteins related to basolateral plasma membrane, focal adhesion, and cell junction (Fig. 2d). Figure 2e shows a predicted ABCC4 PDZ motif-dependent protein network before and after PKA activation. SCRIB and MPP6 were predicted to interact with Avi-ABCC4 even without PKA activation (Fig. 2e, upper panel). Importantly, PKA activation promoted the formation of a more extensive ABCC4-PDZ protein network, including additional PDZ-domain-containing proteins (SCRIB, SNX27, DLG1, MPP6, and MPP2; Fig. 2e, bottom panel). Analytical ultracentrifugation (AUC) using a 15–45% glycerol gradient with computer-controlled small-volume fractionation was used to assess the mass and density of the PKA-driven ABCC4 complexes. A modal peak was observed in both Avi-ABCC4 and Avi-ABCC4 Δ PDZ without PKA activation (fractions 9–13). However, only FL ABCC4 formed a unique large complex, with a median molecular weight >669 kDa around fraction 22 upon PKA activation (Fig. 2f). This finding aligned with the more extensive protein interactions we observed with AP-MS after PKA activation.

From the 37 candidates for ABCC4 interactors, we selected those containing PDZ domains (i.e., SCRIB, SNX27, DLG1, MPP6, and MPP2) to further investigate their interactions with ABCC4 by immunoblot. We first showed that SCRIB and SNX27 interact with Av-ABCC4 in a PDZ-motif dependent fashion by streptavidin pull-down (Fig. 2g, Supplementary Fig. 5a). PKA activation by FSK and IBMX treatment was confirmed by phosphorylation of PKA substrates (Fig. 2g, input panel). A modest increase in ABCC4–SCRIB interaction occurred after PKA activation (Fig. 2g). In addition, co-immunoprecipitation (co-IP) with an ABCC4 primary antibody affirmed endogenous ABCC4 interacts with SCRIB, SNX27, MPP2, and Actin (ACTB), a reported ABCC4 interactor⁷ (Fig. 2h). MPP6 and DLG1 were not detected by either approach, which might be due to the lower sensitivity of immunoblot analysis compared to AP-MS²⁴. We have previously shown a crucial role

of ABCC4 in megakaryopoiesis and the progression of acute myeloid leukemia^{25,26}, as well as the development of a pediatric brain tumor medulloblastoma⁶. Strikingly, by co-IP, we confirmed endogenous ABCC4 interactions with SCRIB, SNX27, and MPP2 in an acute megakaryoblastic leukemia cell line (M-07e) and a medulloblastoma cell line (DAOY) (Supplementary Fig. 5b and c).

SCRIB is a key component in ABCC4 interaction networks

Because SCRIB was a previously uncharacterized interactor of ABCC4, we conducted more detailed investigations into their interaction. Reciprocal co-IPs were performed in cells transiently co-expressing exogenous Flag-tagged SCRIB (Flag-SCRIB) and GFP-ABCC4 variants, using ABCC4 and Flag antibodies (Supplementary Fig. 6a and b). Consistent with earlier observations, the ABCC4–SCRIB interaction relied on the PDZ motif, and this interaction was further enhanced by PKA activation (Supplementary Fig. 6a and b). Confocal microscopy further confirmed the colocalization of ABCC4 and SCRIB, which also increased after PKA activation (Supplementary Fig. 6c). Of note, inhibition of PKA using PKI-14-22 and H89 disrupted the ABCC4–SCRIB interaction, suggesting that PKA activation optimally drives complex formation (Supplementary Fig. 6d).

The detection of SCRIB in some of the fractions as large ABCC4-containing complexes (fractions 21–25) led us to infer that SCRIB was a component of large ABCC4 networks (Supplementary Fig. 7a). No clear enrichment of SCRIB suggested it was a scaffold protein, likely participating with many other protein complexes of similar mass. Therefore, to more directly test if SCRIB is a part of ABCC4-containing assemblies, we employed the crosslinker DSP and omitted DTT (typically used to reverse crosslinking) (Supplementary Fig. 7b). This approach revealed heterogeneous protein complexes organized around ABCC4, dependent on its PDZ motif and consistent with the AUC results (Supplementary Fig. 7b). This finding confirms that SCRIB is a component of the ABCC4 protein network (Supplementary Fig. 7b).

We also investigated the role of SCRIB on ABCC4 plasma membrane localization and function in DAOY cells. SCRIB knock-down by two different siRNAs in DAOY cells markedly reduced both the plasma membrane amount of ABCC4 and correspondingly reduced the resistance to the cytotoxic effects of bis-POM-PMEA (Fig. 3a and b).

APEX-ABCC4 constructs are functional

Next, we investigated if a more extensive PDZ-dependent “neighborhood” of proteins formed near ABCC4 (within ~ 10 nm), both before and after PKA activation. To accomplish this, stable cell lines were developed that express either an ascorbate peroxidase (APEX)-ABCC4 chimera with its PDZ motif (APEX-ABCC4) or without the PDZ motif (APEX-ABCC4 Δ PDZ). APEX catalyzes the formation of biotin-phenol radicals in the presence of hydrogen peroxide from

Fig. 2 | PKA activation promotes ABCC4 PDZ motif-dependent protein complex formation. **a** Scheme depicting ABCC4 biotinylation with Avi-tag and analysis of its interacting proteins. Crosslinker DSP is included in the assay. **b** Medium was collected post-1 h FSK and IBMX treatment and subjected to cAMP ELISA assay to measure the extracellular cAMP concentration. Mean \pm SD of extracellular cAMP levels from 3 independent experiments, normalized to either total protein quantity (left) or surface ABCC4 expression (right) are shown. *** P = 0.001, ** P < 0.01 (p -value = 0.0029), one way ANOVA. * P < 0.05 (p -value = 0.0268), two-tailed Student's t test. **c** Heatmap shows the 37 top hits that interact with ABCC4 through the PDZ motif after PKA activation (SAINT score > 0.9 and FDR < 5%). **d** These top hits were analyzed using the Enrichr database. The bar graph (left) displays the top 10 enriched subcellular components identified through GO Cellular Component 2025 analysis. Enrichr assessed pathway enrichment by Fisher's test (raw p -value

provided), and pathways were ranked by combined score. Graph on the right shows the protein composition of the top 5 subcellular components, with red indicating the presence of a given protein within each term. **e** PDZ motif-dependent ABCC4 interaction networks before (upper panel) and after (lower panel) PKA activation were predicted by STRING. **f** Representative analytical ultracentrifugation-microfractionation of 3 independent experiments. *Fraction 27 represents the bottom eluate. **g** Representative immunoblots (left) show the association of Avi-ABCC4 with SCRIB via its PDZ motif before and after PKA activation. Bars (right) represent mean \pm SD of SCRIB interaction with Avi-ABCC4 (i.e., densitometric of SCRIB pull-down normalized to ABCC4 pull-down) from 3 independent experiments. * p < 0.05 (p -value = 0.0399), unpaired two-tailed Student's t -test. **h** Representative blots from at least 3 independent co-IP assays for endogenous ABCC4 in HEK293 cells.

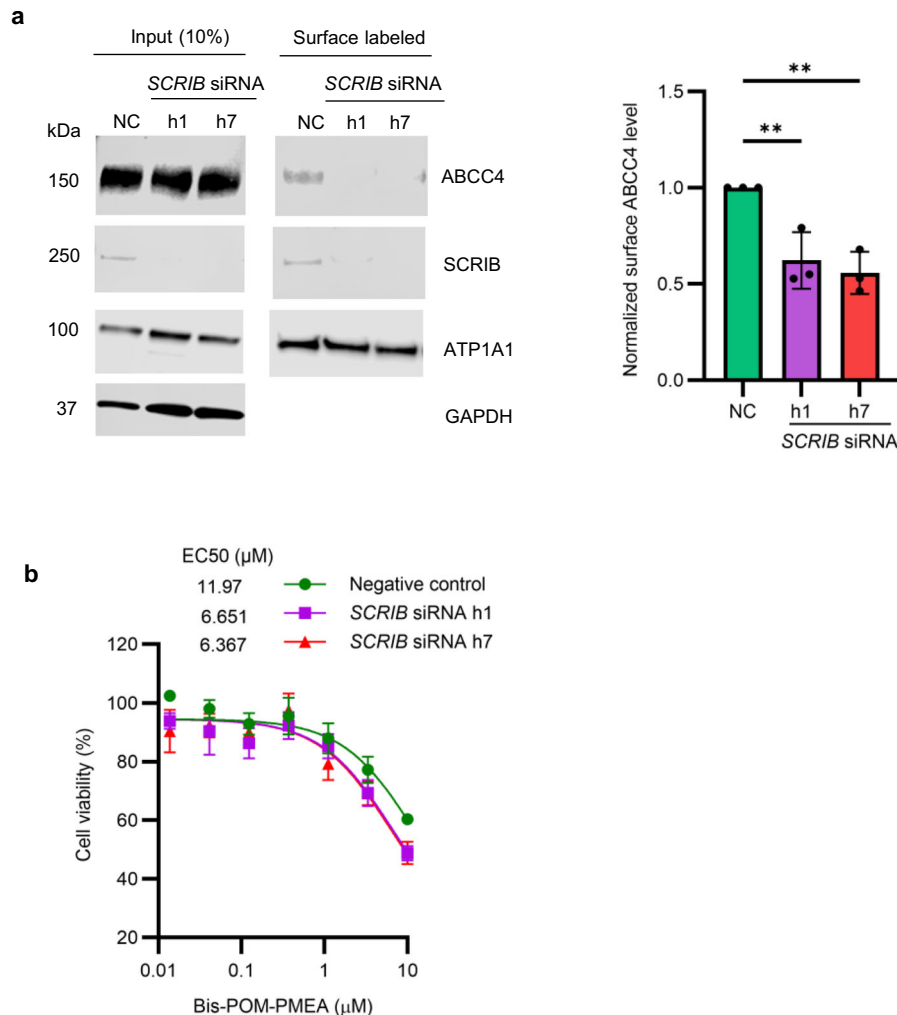
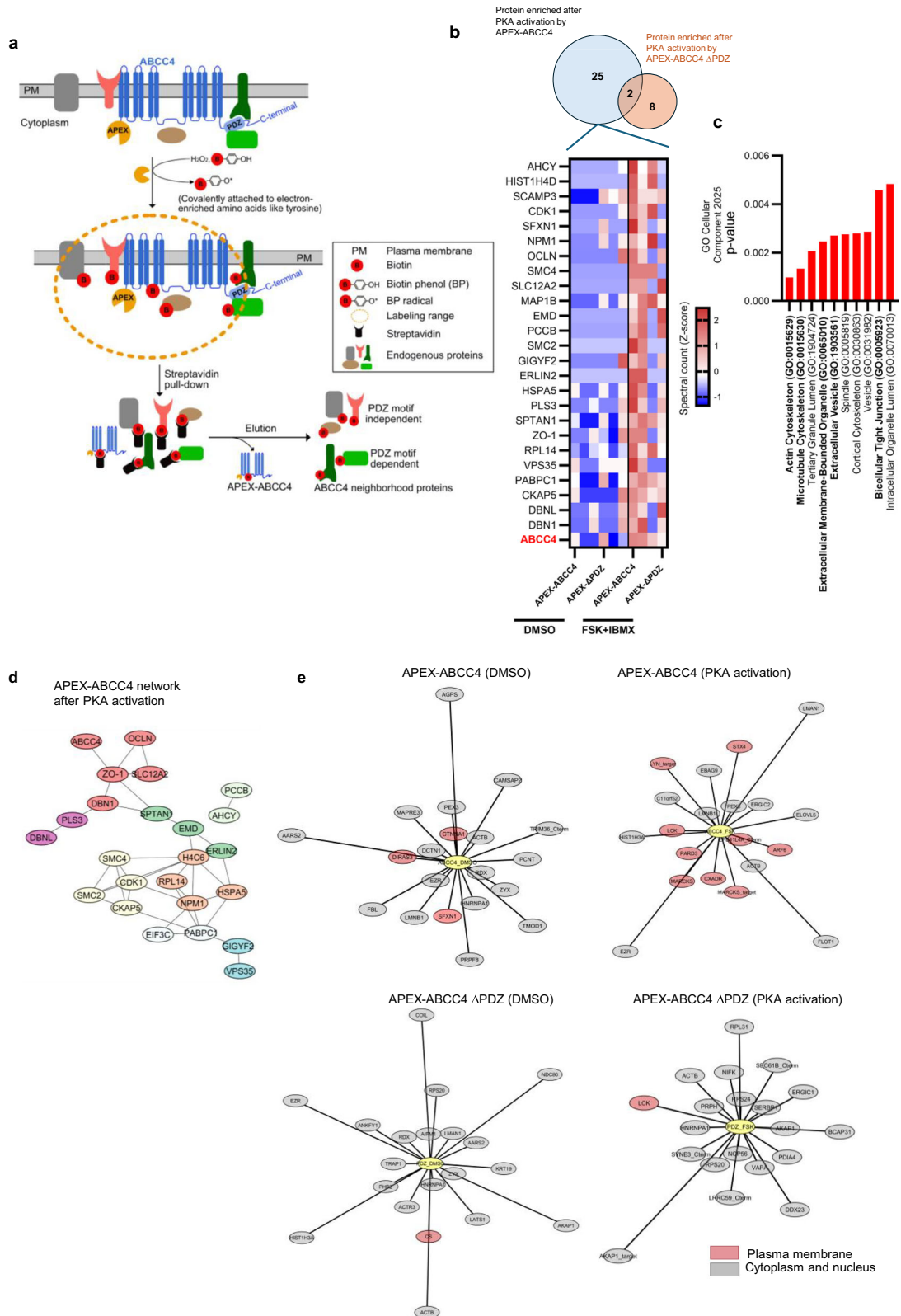


Fig. 3 | Knockdown of SCRIB affects ABCC4 function and membrane localization. DAOY cells were transfected with 25 nM of siRNAs (h1 and h7) targeting human *SCRIB* or a negative control siRNA. **a** Representative immunoblots from 3 independent surface labeling experiments suggest that *SCRIB* suppression markedly reduced the level of ABCC4 in the plasma membrane. Bars (right) represent

mean \pm SD of surface ABCC4 level normalized to surface marker ATP1A1 from 3 biological replicates. ** p < 0.01, one-way ANOVA. p -value = 0.0086 and 0.0040 for h1 and h7, respectively. **b** Cells were treated with different concentrations of Bis-POM-PMEA (0–10 μ M) for 48 h, and cell viability was measured using the CTG assay. Mean \pm SEM of assessed cell viability (%) from 3 biological replicates is shown.

APEX-ABCC4 Δ PDZ (Fig. 4b). SAINT analysis revealed 27 neighborhood proteins significantly upregulated along with APEX-ABCC4 enrichment by PKA activation and 10 with APEX-ABCC4 Δ PDZ (Fig. 4b, Supplementary Table 2). Proteins significantly enriched in the neighborhood of APEX-ABCC4 relied on presence of the PDZ motif as shown in the heatmap (Fig. 4b). Pathway analysis using Enrichr (GO Cellular Component 2025) revealed that these proteins

were primarily related to actin and microtubule cytoskeleton, extracellular vesicles and cell junction (Fig. 4c). Figure 4d shows the network of the significantly enriched proteins predicted by STRING and Cytoscape (Version 3.7.2) in the vicinity of ABCC4. ABCC4 seems to form a network with cell junction proteins (ZO-1, OCLN, DBN1) at the plasma membrane. These cell junction proteins might crosslink ABCC4 with the cytoskeleton proteins (SPTAN1, CKAP5, MAP1B).



These cytoskeletal proteins contribute to the reorganization and stabilization of the actin cytoskeletal network by serving as either actin-bundling proteins (CKAP5)²⁸, actin de-/polymerizing proteins (DBNL)²⁹, or microtubule-actin cross-linkers (MAP1B)³⁰. Importantly, weak PKA activation by isoproterenol treatment was incapable of inducing the accumulation of actin cytoskeleton-related proteins around ABCC4 (Supplementary Fig. 11b).

PDZ motif is required for ABCC4 network growth

Neighborhood proteins of APEX-ABCC4 and APEX-ABCC4ΔPDZ obtained from AP-MS defined the ‘interactome’ of either ABCC4 or itsΔPDZ variant and were then analyzed using the human cell map database (<https://cell-map.org/>). This analysis allowed us to identify proteins (baits with known interactomes in the database) that shared a similar cellular address with our query proteins. Jaccard distance, a set-

Fig. 4 | Proximity labeling by APEX-ABCC4 reveals enrichment of actin cytoskeleton proteins in the presence of ABCC4 PDZ motif and after PKA activation. **a** Scheme of proximity labeling by APEX that was fused to the N-terminus of ABCC4. **b** SAINT analysis revealed 27 and 10 proteins enriched in the neighborhood of APEX-ABCC4 and APEX-ABCC4 DPDZ, respectively. The heatmap shows the bait protein ABCC4 and 25 hits that are significantly enriched after PKA activation and specific to the PDZ motif (SAINT score > 0.85 and FDR < 5%). **c** Pathway enrichment analysis (Enrichr, GO Cellular Component 2025) of these 25 neighborhood proteins revealed that the Actin cytoskeleton proteins were enriched the most. Pathway enrichment was assessed using Fisher's test (*p*-value provided) as implemented in

Enrichr, with results ranked by combined score. **d** The protein cluster diagram of ABCC4 and top neighborhood hits was generated by using the STRING database and Cytoscape (version 3.7.2). **e** Protein similarity analysis was performed using the human cell map database. Node-edge diagrams represent the top 20 proteins whose interactomes are most similar to that of APEX-ABCC4 or APEX-ABCC4 DPDZ before and after PKA activation. Length of edges is inversely proportional to the degree of similarity with the query protein. Color represents the expected cellular location of these in the database (red: plasma membrane and gray: cytoplasm or nucleus). The protein network was created using an edge-weighted spring-embedded layout in Cytoscape (version 3.7.2).

based dissimilarity metric, was used to quantify this localization. The calculated Jaccard index (Jaccard index = 1 - Jaccard distance) was a measure of overlap. Figure 4e showed the top 20 baits most similar to either APEX-ABCC4 or APEX-ABCC4 ΔPDZ, before and after PKA activation. Each node was color-coded by its known subcellular localization, and edges represent the degree of interactome similarity to the query protein, as determined by the Jaccard index. It was noted that ACTB was one of the most-similar baits with ABCC4 but was much less similar to ABCC4ΔPDZ location, which supports our hypothesis that ABCC4 assembly with the actin cytoskeleton relies on its PDZ motif (Fig. 4e). Interestingly, PKA activation induced marked changes in the proximity-based similarity network for APEX-ABCC4, but not for the ΔPDZ variant (Fig. 4e). This suggests two possible mechanisms: (1) a large PKA-dependent shift in ABCC4 localization toward the plasma membrane, or (2) a reorganization of ABCC4 local environment without a change in compartment. Because surface labeling confirmed that both ABCC4 forms were present at the plasma membrane regardless of PKA activation (Supplementary Fig. 8c), these findings are more likely to reflect that PKA activation promotes remodeling of ABCC4's protein network, and that this reorganization is dependent on the PDZ motif.

Cee4ourin 2 destabilizes ABCC4 and affects its local networks

Cee2 is a potent ABCC4 inhibitor uncovered through high-throughput screening, but its mechanism is still unclear. We first assessed if Cee2 altered the localization of ABCC4. Both fluorescence microscopy and iodixanol gradient centrifugation indicated that ABCC4 remained in the plasma membrane compartment following Cee2 treatment (Supplementary Fig. 9a and b). However, interestingly, surface labeling revealed a noticeably smaller proportion of ABCC4 at the plasma membrane after 24 h of Cee2 treatment (Supplementary Fig. 9c). These findings suggest that Cee2 does not necessarily relocate ABCC4 but may transiently alter its conformation, thereby reducing the accessibility of extracellular epitopes to surface-labeling reagents or inducing faster internalization.

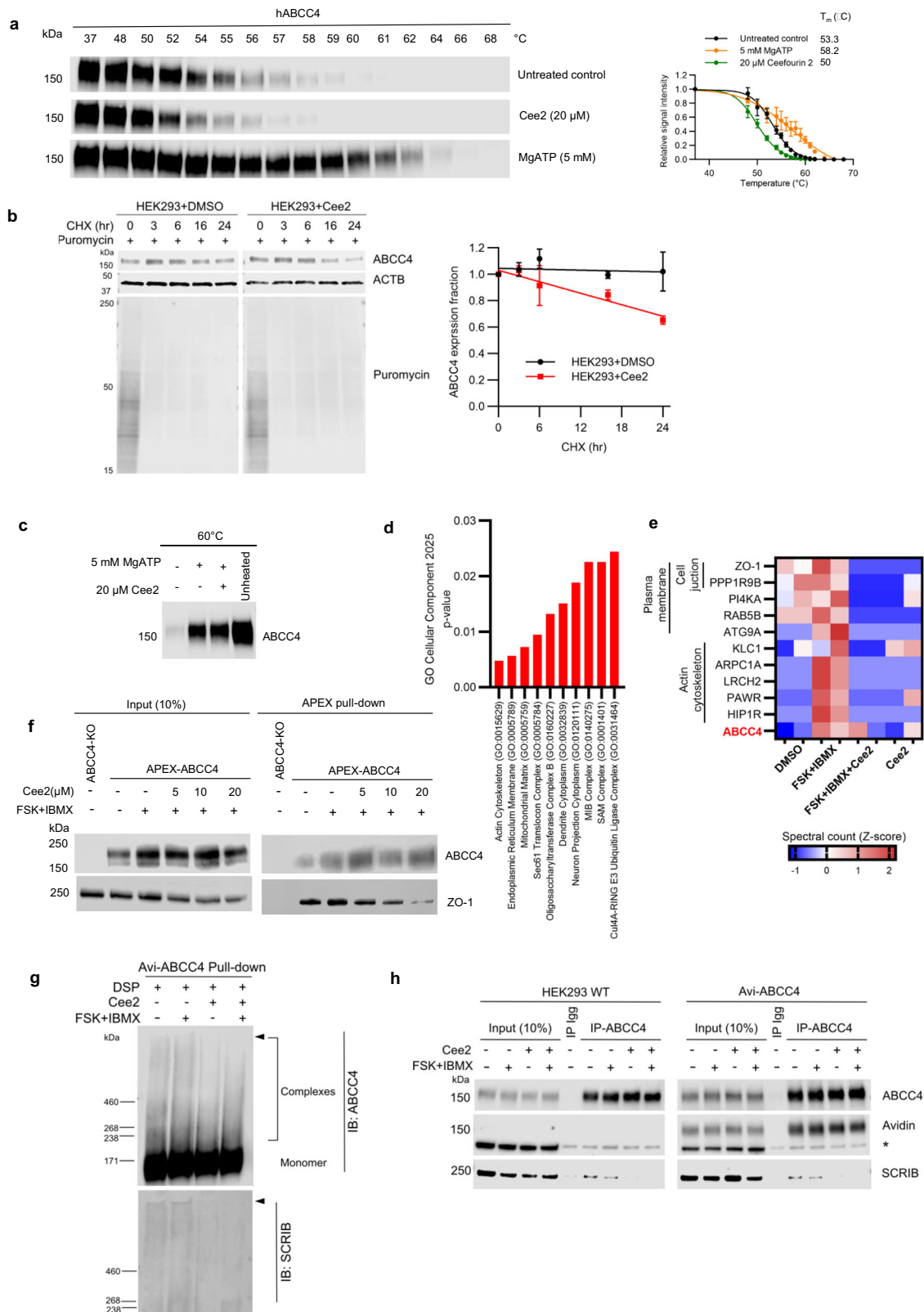
We and others have shown that inhibitors, when bound to transporters, stabilize them against thermal denaturation^{31–33}. Using a membrane thermal shift assay as a proxy for ligand binding, we investigated whether ABCC4 was thermally stabilized by the inhibitor Cee2. ABCC4 mediates export through binding ATP to its nucleotide-binding domain³⁴. Magnesium ATP (MgATP) was used as a positive control for ligand binding to ABCC4. As expected, MgATP treatment produced a strong (4.9 °C) increase in the T_m over that of the untreated control (53.3 °C) (Fig. 5a). Cee2 treatment did not produce thermal stabilization. Instead, it produced an unexpected modest (3.3 °C) reduction in the T_m (Fig. 5a). This reduced T_m could result from weak binding between ABCC4 and Cee2, which occurs with some inhibitors of ABCB1³⁵, or from a destabilized ABCC4–Cee2-binding complex. Consistent with this finding, protein turnover assay with CHX treatment suggested that Cee2 treatment slightly decreased the half-life of ABCC4 in HEK293 cells (Fig. 5b). A previous study reported that P-glycoprotein inhibitors (such as tariquidar and zosuquidar) interfere with ATP binding to its nucleotide domain³⁵. We determined whether Cee2 had effects similar to those of P-glycoprotein inhibitors. Cee2

treatment did not affect ATP-induced thermal stabilization of ABCC4 (Fig. 5c).

We hypothesized that Cee2 affected ABCC4 stability and function by altering its local network. We investigated whether Cee2 influences the neighborhood of APEX-ABCC4 using AP-MS. SAINT analysis was performed to identify ABCC4-proximal proteins significantly altered by Cee2 treatment (Supplementary Table 3). Strikingly, Enrichr and Gene Ontology (GO) pathway analyses of these candidates (SAINT score > 0.9 and FDR < 5%) revealed that Cee2 strongly reduced the presence of actin cytoskeleton-related proteins in the ABCC4 environment (Fig. 5d) and significantly altered actin-associated proteins, plasma membrane proteins and cell junction proteins were shown in the heatmap in Fig. 5e. Of note, Cee2 did not cause widespread disruption of the entire ABCC4-proximal proteins (Supplementary Fig. 10a). Because ZO-1 was the top proximal protein candidate disrupted by Cee2, we further evaluated Cee2 effect on ZO-1 by immunoblot. ZO-1 enrichment via APEX-ABCC4 labeling was reduced by Cee2 in a dose-dependent manner (Fig. 5f). We then assessed Cee2's impact on ABCC4 network by Avi-ABCC4 pull-down experiments under crosslinking conditions (using DSP in the absence of DTT). Cee2 markedly reduced the presence of high-molecular-weight ABCC4-containing complexes, particularly those >460 kDa, before and after PKA activation (Fig. 5g). Unfortunately, ZO-1 was undetectable using this approach, possibly due to a much shorter distance (~10-fold) DSP could crosslink compared to the APEX-labeling radius. Nonetheless, SCRIB involvement in these ABCC4 large complexes was confirmed and found to be diminished by Cee2 (Fig. 5g). In line with this finding, we showed Cee2 treatment disrupted the interaction between ABCC4 and SCRIB by co-IP using ABCC4 antibody in multiple cell systems, including HEK293 WT cells, cells stably expressing Avi-ABCC4 and cells transiently co-expressing GFP-ABCC4 and Flag-SCRIB (Fig. 5h, Supplementary Fig. 10b). Importantly, the reduction of the ABCC4–SCRIB interaction by Cee2 was also observed in M-07e cells but unexpectedly not in DAOY cells (Supplementary Fig. 6b and c).

Discussion

Our results reveal that PKA-mediated increases in cAMP drive ABCC4 to the plasma membrane with concomitant increases in cAMP efflux, and that this is associated with the formation of high molecular weight ABCC4 protein complexes mostly dependent upon its PDZ motif. We elucidated ABCC4 protein complexes composition by employing either an Avi-tagged ABCC4 (containing) or lacking the PDZ motif to capture ABCC4 protein interactors. We demonstrated that PKA activation promotes the formation of large protein complexes involving PDZ proteins. Loss of the PDZ motif disrupted this PKA-induced protein complex, suggesting that the PDZ motif is vital for the integrity of the ABCC4 protein complex. Proximity labeling of proteins in the vicinity of ABCC4 with an APEX-tagged ABCC4 then offered insight into ABCC4 microenvironment with extended distance, which indicated that ABCC4 connects, driven by PKA, to the actin cytoskeleton. We propose a model whereby PKA activation increases ABCC4 localization to the membrane (Fig. 6). Surprisingly, ABCC4 inhibition by Cee2 does not just inhibit cAMP export by ABCC4 but also disrupts its



actin cytoskeletal network by affecting interactions of some key proteins.

One previously undiscovered ABCC4 interactor uncovered by our study is SCRIB, which is profoundly involved in ABCC4-containing complexes. SCRIB genetic suppression revealed that SCRIB seems to play a key role in ABCC4 localization and function. Because the extent of the response to PKA hyperactivation (induced by short-term FSK

and IBMX treatment) differed between exogenous and endogenous ABCC4, the pattern of ABCC4–SCRIB interaction modulated by PKA hyperactivation also varied between these cell systems. However, it is convincing that PKA activation is required for ABCC4–SCRIB interaction to occur, as this interaction was diminished when PKA was inhibited. Other PDZ motif-interacting proteins, such as membrane palmitoylated proteins (MPPs), which have previously been reported

Fig. 5 | Ceefourin 2 affects the ABCC4 network. **a** Representative immunoblots demonstrate assessment of ABCC4 melting temperature (T_m) (left). Mean \pm SEM of densitometry quantification of ABCC4 from 4 biological replicates of untreated control and 3 biological replicates of MgATP and Cee2 groups are shown on the right. **b** HEK293 cells were treated with DMSO or 20 μ M Cee2 for 24 h, with CHX added at intervals to assess ABCC4 turnover and puromycin added 10 min before harvest. Representative immunoblots from 3 independent experiments are shown on the left. Graph (right) shows the assessed half-lives of endogenous ABCC4 with or without Cee2 treatment (mean \pm SD). **c** Representative blot from 4 independent experiments shows ATP interaction with ABCC4 with or without Cee2. **d** Hyper-PKA-activation-induced ABCC4 neighborhood proteins significantly reduced by Cee2 were analyzed in GO Cellular Component 2025 analysis (Enrichr), where pathway enrichment was assessed by Fisher's test and ranked by combined score. The top 10 terms and their raw p -value are shown. **e** ABCC4 neighborhood proteins significantly changed by Cee2 (see Supplementary Table 3) were sorted based on

their subcellular localization. The heatmap showed those at the plasma membrane, cell junction, or actin cytoskeleton. **f** APEX-ABCC4 treated with 20 μ M Cee2 or DMSO for 24 h, with FSK and IBMX added 4 h before endpoint. Post APEX activation, cell lysates were subjected to affinity pull-down. Representative immunoblots from 2 independent experiments are shown. **g** Avi-ABCC4 cells were treated with 20 μ M Cee2 or DMSO for 48 hours, with FSK and IBMX added 4 h before endpoint. Cells were subjected to crosslinking and affinity pull-down. Arrows point out a visible protein complex containing ABCC4 and SCRIB, which was dramatically affected by the addition of Cee2. Representative blots of 3 independent experiments are shown. **h** HEK293 WT or Avi-ABCC4 cells were treated with 20 μ M Cee2 or DMSO for 48 h, with FSK and IBMX included for 4 h before the Cee2 treatment endpoint. Co-IP was performed to assess SCRIB interaction with ABCC4. Representative blots of 2 independent experiments are shown. *Indicates a non-specific band of endogenous biotinylated protein.

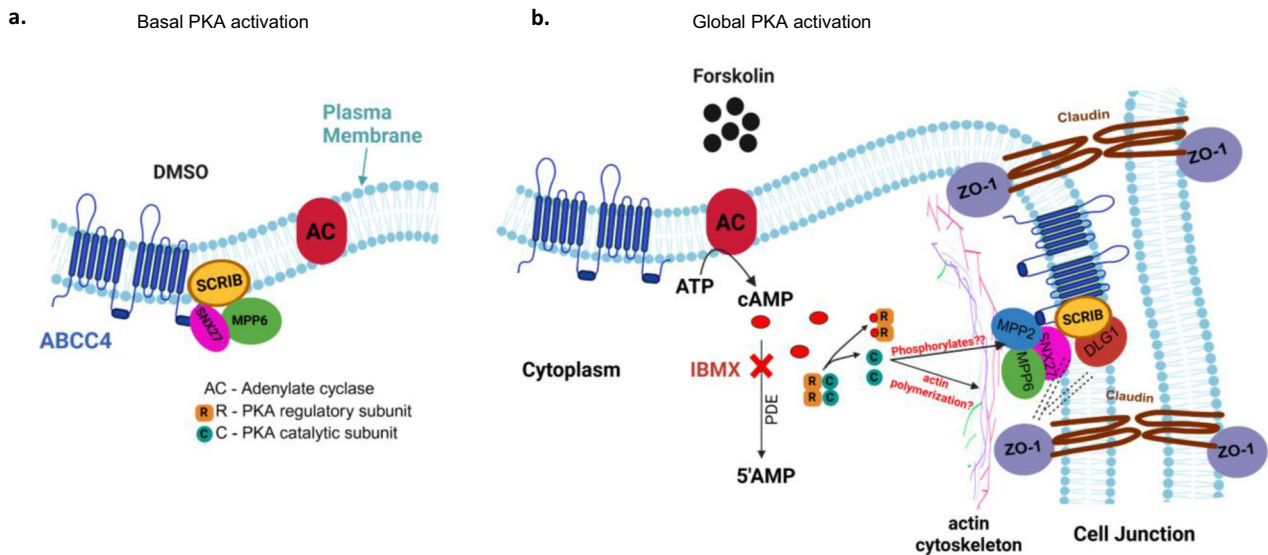


Fig. 6 | PKA activation promotes ABCC4 plasma membrane localization by inducing the formation of ABCC4 PDZ motif-dependent complex and by concentrating actin cytoskeletal proteins near ABCC4. **a** Under basal PKA signaling conditions, ABCC4 interacts with PDZ proteins (SCRIB and MPP6) via its PDZ motif, which may facilitate tethering of ABCC4 to the plasma membrane. **b** Treatment of FSK and IBMX causes global activation of cAMP/PKA signaling. Global PKA

activation increases localization of ABCC4 at the plasma membrane microdomains by enhancing the formation of ABCC4 macromolecular complex and by promoting the enrichment of actin cytoskeletal proteins and cell junction proteins near ABCC4. This macromolecular complex possibly stabilizes ABCC4 by acting as a cross-linker between ABCC4 and the actin cytoskeleton. Figure was created in BioRender. Zhu, J. (2025) <https://BioRender.com/57999d7>.

to interact with proteins belonging to the polarity complex, such as ZO-1 and DLG1, appear to contribute to network formation too³⁶. MPPs provide a link between the cell membrane proteins and the cytoskeleton, especially when interacting with the 4.1 superfamily³⁶. Supportively, several 4.1 superfamily proteins like EPB41L2 and EPB41L3 were found among the top hits for Avi-ABCC4 interactors. Interrogation of the BioGRID database further shows that actin interactions can occur through cell junction proteins like SCRIB, DLG1, and ZO-1 (<https://thebiogrid.org/>). The PDZ-binding protein SNX27 reportedly has a role in ABCC4 internalization³⁷. Further studies are needed to interpret SNX27's role in ABCC4 networks, particularly after PKA activation. Cumulatively, our findings are consistent with the idea that PDZ proteins tether ABCC4 to the membrane and reduce its mobility to promote function.

By assessing ABCC4's thermal stability using a thermal shift assay, we demonstrated that the potent and specific ABCC4 inhibitor Cee2 neither thermally stabilized ABCC4 nor interfered with ATP-induced ABCC4 thermal stabilization, which was puzzling given its strong inhibitory potency¹⁹. Furthermore, the discordance in Cee2's effect on ABCC4 localization revealed by different assessments may suggest that Cee2 caused a potential conformational change of ABCC4. Since

no evident thermal stabilization was seen in ABCC4–Cee2, whether this conformational change exists or whether it is through direct binding is still unclear. However, this potential conformational change may explain the disruption of ABCC4's ability to engage with cytoskeletal protein networks observed in APEX-ABCC4 and Avi-ABCC4 cells from our study—an effect reminiscent of the functional impairments caused by PDZ motif loss. Disruption of ABCC4-interacting networks may represent an uncharacterized or partial mechanism by which Cee2 inhibits ABCC4. We speculate that other transport inhibitors that do not strongly and physically interact with their target transporters but nonetheless inhibit their function might behave similarly.

Together, our findings show that PKA does not merely localize ABCC4—it organizes a PDZ-dependent membrane neighborhood that tethers the transporter to actin/junction modules, constrains its lateral mobility, and stabilizes surface pools to optimize cAMP efflux. By delineating the underlying protein machinery—including a previously unrecognized role for SCRIB—this work provides a mechanistic blueprint for microdomain control of nucleotide signaling. The neighborhood is functionally required: disrupting the ABCC4 PDZ motif or depleting SCRIB destabilizes surface ABCC4, accelerates diffusion, and attenuates PKA-stimulated cAMP export. Pharmacologically, the

selective inhibitor Ceefourin-2 impairs ABCC4 not by canonical target stabilization but by dismantling neighborhood integrity, shifting the focus from transporter-centric to network-centric inhibition. These results nominate PDZ–scaffold interfaces and neighborhood stability as tractable intervention points in contexts where PKA signaling and ABCC4 activity are heightened, and they establish a broadly applicable framework—proximity mapping, single-molecule diffusion, and thermal profiling—to resolve and modulate microdomain organization across ABC transporters.

Methods

Development of HEK293 *ABCC4*-KO cells by CRISPR-Cas9

HEK293 cells were transfected with CRISPR-Cas9 vector U6gRNA-Cas9-2A-GFP containing gRNAs targeting human *ABCC4* (CCAACCCGCTG-CAGGACGCGAA, Sigma Aldrich). Post 48 h of transfection, the top 10% GFP-positive single cells were sorted into each well of a 96-well plate and expanded. A single clone that has a stable deletion of *ABCC4* from HEK293 cells was confirmed by immunoblotting and used for follow-up studies.

Cloning and site-directed mutagenesis

Human *ABCC4* with an N-terminal GFP tag was generated by cloning *ABCC4* into a pAC-GFP vector (Clontech Laboratories). Avi-*ABCC4* construct was generated by cloning the human *ABCC4* cDNA into pReceiver-M48 vector (GeneCopoeia) containing the insert N-Avi and IRES biotin ligase. APEX-*ABCC4* construct was generated by cloning the human *ABCC4* gene into pCDNA3.1 vector containing the insert flag and APEX (Addgene).

Δ PDZ variant for *ABCC4* in these constructs was developed by introducing a single mutation that leads to an early stop codon before the PDZ motif using a QuikChange II XL site-directed mutagenesis kit (Stratagene). Sequences of primers used for mutagenesis are shown below. Sequences of constructs were confirmed by DNA Sanger sequencing.

Forward primer: 5'-CCTCGACCTTAAGTATTTTCTAGACAGCACT GT GACCGCGG-3';

Reverse primer: 5'-CCGCGGTACAGTGTCTAGAAAATAGTT AAGGTCGAGG-3'.

Generation of stable cell lines

Construct containing Avi-*ABCC4*, Avi-*ABCC4* Δ PDZ, APEX-*ABCC4*, or APEX-*ABCC4* Δ PDZ was transfected individually into HEK293 *ABCC4*-KO cells using Lipofectamine 2000. G418 (2 mg/ml) and bis-POM-PMEA (2.5 μ M) were added at 48 h post-transfection to select cell colonies that stably expressed *ABCC4* variant.

Cell culture

HEK293 WT or its derived cell lines were cultured in Dulbecco's modified Eagle's medium (DMEM) supplemented with 10% fetal bovine serum (FBS) and 2 mM L-glutamine, 1% penicillin/streptomycin. DAOY cells were cultured in Eagle's minimum essential medium (MEM) containing 10% FBS, 2 mM glutamine, and 1% penicillin/streptomycin. M-07e cells were cultured in RPMI 1640 medium supplemented with 10% FBS, 2 mM L-glutamine, and 1% penicillin/streptomycin. All the cells were incubated in a humidified incubator at 37 °C supplied with 5% CO₂.

cDNA plasmid transfection

HEK293 *ABCC4*-KO cells were transiently transfected with plasmids by using Lipofectamine 2000 (Thermo Fisher), following the manufacturer's protocol. Briefly, 0.3×10^6 cells were seeded per well in a six-well plate. After 24 h of incubation, cells were transfected with DNA-lipofectamine 2000 complex in reduced-serum Opti-MEM media. The media was changed after 24 h, and the cells were further incubated for another 24 h before harvesting.

siRNA transfection

Avi-*ABCC4* and APEX-*ABCC4* cells (1.2×10^6 cells/flask) were seeded in T-25 flasks. The cells were transfected with either negative-control siRNA or *SCRIB* siRNAs from Qiagen: Hs_*SCRIB_1* siRNA (Cat. # SIO0712635) or Hs_*SCRIB_7* (Cat. # SIO4295655) using Lipofectamine 2000 per the manufacturer's protocol. First, 25 nM of siRNA was complexed with 5 μ L of Lipofectamine 2000 in Opti-MEM media. The cells were then incubated with siRNA-lipofectamine complex overnight; the media was changed the following day. After incubation for another 24 h, the cells were processed as needed.

TIRF live-cell imaging

HEK293 *ABCC4*-KO cells were seeded on 4-well chambered cover-glass slides (LAB-TEK). After 48 h, the cells were transfected using Lipofectamine 2000 with plasmid DNA (0.25 μ g) encoding either GFP-*ABCC4* or GFP-*ABCC4* Δ PDZ. The cells were visualized under the Marianas system (Intelligent Imaging Innovation) configured with an EMCCD high-sensitivity camera. The images were taken using a $\times 100$ Zeiss objective and the 488-laser line. Single particles were tracked and analyzed using Imaris (Bitplane).

Confocal live-cell imaging and analysis

To avoid cell detachment, iBidi cell chambers were coated with poly-L-lysine. HEK293 *ABCC4*-KO cells were then seeded, and when 50% confluent, cells were transfected with GFP-*ABCC4* or GFP-*ABCC4* Δ PDZ using Lipofectamine 2000. After 48 h of DNA transfection or after compound treatment as indicated, 3D images were taken by Marianas spinning disk confocal microscopy with $\times 63$ or $\times 100$ oil lens in a chamber at 37 °C, and with 5% CO₂. GFP signal was monitored by confocal-488 laser line. WGA-Alexa Fluoro 647 staining was included 5 min before imaging and recorded by confocal-640 laser line.

To quantify the GFP dynamics over time, images were imported into Fiji ImageJ software. To unbiasedly remove the background fluorescence, the image threshold was adjusted using the percentile. The sum of GFP intensities in each Z-stack was divided by the total number of cells in a field to calculate GFP *ABCC4* expression at each timepoint.

Immunofluorescence

#1.5 coverslips were placed into 12-well plates and coated with poly-L-lysine before the experiment. 24 h after HEK293 Avi-*ABCC4* cells were seeded, they were fixed with 4% paraformaldehyde, washed twice with phosphate-buffered saline, pH 7.4 (PBS), and permeabilized by incubation with PBS containing 0.1% saponin for 15 min. The cells were then blocked by incubation with permeabilization solution containing 5% BSA for 1 h at RT. To visualize Avi-*ABCC4*, cells were incubated with Streptavidin Alexa Fluor 488 (1:1000) in permeabilization solution containing 1% bovine albumin serum (BSA) for 1 h, while *SCRIB* (1:250) primary antibody was incubated in the same buffer solution overnight and washed 3 times with PBS for 5 min per wash. The cells were then incubated with Alexa Fluor 647 goat anti-mouse (1:500) secondary antibodies for 1 h and washed three times with permeabilization solution. The coverslips containing the cells were then mounted onto the glass slide by using Prolong Gold antifade mount with DAPI. The coverslip was allowed to dry for at least 72 h. Imaging was performed in Marianas spinning disk confocal microscope with $\times 63$ oil objective, using confocal-488 and 640 laser lines.

Cell-line drug sensitivity studies

HEK293 *ABCC4*-KO cells with Avi- or APEX-*ABCC4* variant construct were seeded at 1000 cells per well in a 96-well plate. After overnight incubation, the cells were treated with different concentrations of drugs (9-(2-((Bis((pivaloyloxy)methoxy)phosphinyl) methoxy)ethyl) adenine(bis-POM-PMEA), irinotecan, and mitoxantrone. The cell viability was measured after 72 h by using the CellTiter-Glo luminescent

cell viability assay (Promega), following the manufacturer's instructions. The dose–response curve and EC50 values were determined by using GraphPad Prism.

cAMP ELISA assay

ABCC4 variant-expressing cells were seeded at 5×10^5 cells per well in a six-well plate. After 48 h, cells were incubated with FSK (50 μ M) and IBMX (100 μ M) for 1 h to concentrate cAMP. Medium was collected to measure extracellular cAMP level using a cAMP complete ELISA kit (Enzo, Cat. # ADI-900-163A), following the manufacturer's instructions. The calculated cAMP levels were normalized to total protein quantity and membrane protein expression level obtained through immunoblotting.

Immunoblotting

The cells were lysed in RIPA lysis buffer containing the following protease inhibitors: 1x EDTA-free protease inhibitor cocktail (Roche), 1 mM phenylmethylsulfonyl fluoride (PMSF), 10 mM N-ethylmaleimide (NEM), and 1 μ M MG132. The cell lysates were incubated on ice for 30 min and vortexed every 10 min for 5 s. The protein lysate was separated from the cell debris by centrifugation at $10,000 \times g$ for 5 min. The concentration of the protein was quantified via the BCA protein assay. Equal amounts of proteins were mixed with SDS sample buffer containing 20 mM DTT and loaded into a 4–15% gradient polyacrylamide gel, subjected to SDS–PAGE gel electrophoresis. Proteins in the gel were transferred to a nitrocellulose membrane. Blots were blocked with 5% non-fat milk in TBST (5% milk) at RT for 1 h. Primary antibodies (see details in Supplementary Table 4) were diluted in 5% milk and incubated with the blot overnight at 4 °C. Secondary antibodies were incubated for 1 h at room temperature (RT) on the next day. The Bio-Rad Clarity™ western ECL chemiluminescence substrate (Bio-Rad, Cat. #1705061) or SuperSignal™ west femto maximum sensitivity substrate (Thermo Scientific, Cat. #34096) was used to detect proteins.

Cell surface labeling

Cells were washed with cold PBS and incubated with 0.25 mg/ml of Sulfo-NHS-SS-Biotin solution in PBS at 4 °C for 30 min, with gentle rocking. The excess of labeling reagent was quenched by incubating the cells in 5 mM Tris–HCl (pH = 7.5). The cells were then harvested and lysed in RIPA lysis buffer (Pierce) containing protease inhibitors as depicted above. Protein quantity in the cell lysate was measured via BCA protein assay and calibrated to 1 mg/ml. Streptavidin-agarose beads (Pierce, Cat. #20353) were used for affinity pull-down of biotinylated cell surface proteins. Beads were incubated with cell lysates with a 1:3 volume ratio overnight on a rotator at 4 °C. The next day, 10% flow-through (FT) was saved. Beads were then washed with RIPA buffer three times, and proteins were eluted with 3x SDS sample buffer containing 50 mM DTT and 10 mM biotin by heating at 37 °C for 30 min. The input (10%) and the total eluate, 10% FT, were analyzed by immunoblotting.

Proximity labeling by APEX

HEK293 ABCC4-KO cells stably transfected with APEX-tagged ABCC4 with or without a PDZ motif were seeded in a 10-cm dish. When confluent, cells were incubated in fresh media containing 50 μ M FSK and 100 μ M IBMX for indicated intervals, followed by incubation with 500 μ M biotin-phenol for 30 min at 37 °C and with 1 mM H₂O₂ for 1 min at RT. The biotinylating reaction was quenched by washing the cells three times with PBS containing antioxidants (10 mM sodium ascorbate, 10 mM sodium azide, and 5 mM Trolox).

Affinity pull-down of Avi-tag and APEX-tag

Avi-tagged cells or APEX-activated cells were harvested and lysed. To enrich biotinylated proteins, cell lysates calibrated to 1 mg/ml were

incubated with streptavidin-agarose beads (volume ratio 2.5–3:1) overnight with rotation at 4 °C. The next day, protein lysates were separated from beads by centrifugation at $2000 \times g$ at 4 °C. Beads were then washed twice with RIPA buffer, and once with 1 M KCl and once with 0.1 M NaHCO₃ (by incubating with each buffer for 5 min at 4 °C, followed by centrifugation). The biotinylated proteins were eluted from the beads with 4X LDS sample buffer containing 50 mM DTT and 2 mM biotin at (1) 95 °C for 5 min for MS analysis or (2) 37 °C for 30 min for immunoblot analysis alone.

To visualize the ABCC4 networks by immunoblot, Avi-tagged cells were crosslinked with 0.5 mM DSP with very gentle rocking at RT for 30 min before lysis and affinity pull-down. Proteins were eluted in 3x SDS sample buffer containing 20 mM biotin at 37 °C for 30 min and subjected to 3–8% Tris–Acetate (Bio-Rad, #3450130) PAGE.

Sample preparation and mass spectrometry

Protein samples were run on a short gel as described in a previously published protocol³⁸. Proteins in gel bands were reduced with DTT and alkylated by iodoacetamide (IAA) (Sigma). The gel bands were then washed, dried, and rehydrated with a buffer containing trypsin (Promega). Samples were digested overnight, acidified, and the peptides were extracted. The extracts were dried and reconstituted in 5% Formic acid. The peptide samples were loaded on a nanoscale capillary reverse phase C18 column (Thermo Easy Spray (ES904) 75id, 2 μ m C18, 150 mm) by an HPLC system (Thermo Ultimate 3000) and eluted by an acetonitrile gradient. The eluted peptides were ionized and detected by an inline mass spectrometer (Thermo Orbitrap Exploris 480). The MS and MS/MS spectra were collected over a 75-min liquid chromatography gradient. The mass spectrometer is operated in data-dependent mode with a survey scan in Orbitrap (60,000 resolution, 1E6 AGC target and 50 ms maximal ion time) and MS/MS high resolution scans (15,000 resolution, 1E5 AGC target, 150 ms maximal ion time, 32 HCD normalized collision energy, 1.5m/z isolation window, and 8 s dynamic exclusion).

Database search and analysis

Database searches were performed using JUMP³⁹ search engine against a composite target/decoy Uniprot human protein database⁴⁰. Searches were performed using a 25 ppm mass tolerance for precursor and fragment ions, fully tryptic restriction with two maximal missed cleavages. Carbamidomethylation of Cysteine (+57.02146 Da) was used for static modification, and Met oxidation (+15.99492 Da) was considered as a dynamic modification. All matched MS/MS spectra were filtered by mass accuracy and matching scores to reduce the protein false discovery rate to <1%. Spectral counts, matching to individual proteins, reflect their relative abundance in one sample after the protein size is normalized. The spectral counts between samples for a given protein are used to calculate the *p*-value, which is derived by the *G*-test⁴¹. Interaction candidates were detected using Significance analysis of interactome (SAINT) express software²³ with default parameters. Proteins with SAINT score > 0.9 or 0.85 and Bayesian false discovery rate (FDR) < 5% were considered as interaction candidates.

The mass spectrometry proteomics data have been deposited to the ProteomeXchange Consortium⁴² via the PRIDE^{43,44} partner repository with the dataset identifier [PTX048010](https://doi.org/10.6019/PTX048010).

Co-immunoprecipitation

Cells were lysed in M-PER buffer containing protease inhibitors, as shown in the “Immunoblotting” subsection. Protein concentration was measured by BCA and calibrated to 1 mg/ml. 150–300 μ g of protein lysate was incubated with 2–5 μ g primary antibody (polyclonal, rabbit anti-ABCC4 (in-house) or monoclonal mouse anti-Flag M2 (Sigma)) overnight in a rotator at 4 °C. An equal amount of control IgG antibody from the same species was used as a control. The next day, 20–40 μ l of Protein G PLUS-agarose beads (Santa Cruz) slurry was used per

150–300 μg protein. The antibody–protein suspension was incubated with the washed Protein G PLUS-agarose beads (Santa Cruz, sc-2002) for 3 h in a rotator at 4 °C. Beads were washed three times with the lysis buffer. The immunoprecipitated proteins were eluted from the beads by heating in 3 \times SDS or 4 \times LDS sample buffer containing 50 mM DTT at 37 °C for 30 min and analyzed by immunoblot.

Cycloheximide chase assay

Cells with indicated treatment were treated with cycloheximide (CHX, 10 $\mu\text{g}/\text{ml}$) at different intervals from 0 to 24 h. Puromycin (10 $\mu\text{g}/\text{ml}$) was added to the cells for 10 min before harvesting. Puromycin is incorporated into newly synthesized proteins, and the extent of protein translation can be verified by using anti-puromycin antibody⁴⁵. We used puromycin to verify CHX effectiveness.

Iodixanol density gradient ultracentrifugation

Separation of plasma membrane, endoplasmic reticulum (ER), and lysosomal fractions was performed using iodixanol density gradient ultracentrifugation as previously described^{46,47}. Briefly, cells were washed with PBS and centrifuged at 1000 $\times g$ for 5 min at 4 °C. Cells were homogenized in homogenization medium, HM (25 mM Tris pH 7.4, 250 mM Sucrose, 1 mM EDTA) using a Dounce homogenizer. The homogenate was centrifuged at 500 $\times g$ for 5 min, which pelleted cell debris and nuclei. The supernatant, which contained plasma membrane and other organelles, was then pelleted by ultracentrifugation at 100,000 $\times g$ for 30 min at 4 °C, using Beckman Coulter Optima™ Max-XP Ultracentrifuge. The resulting pellet was resuspended in the HM buffer and layered over a 10–30% iodixanol gradient and centrifuged at 100,000 $\times g$ overnight at 4 °C. Equal volumes of 24 fractions were collected from top to bottom, and protein expression was detected by immunoblotting.

Glycerol gradient analytical ultracentrifugation (AUC)-microfractionation

Avi-ABCC4 and Avi-ABCC4 ΔPDZ cells were treated with FSK (50 μM) and IBMX (100 μM) or DMSO for 4 h. The cells were then harvested and cross-linked by incubating them in 2 mM DSP solution in PBS at RT for 30 min. The excess cross-linker was quenched by incubating the cells in 20 mM Tris–HCl, pH 7.5 in PBS at RT for 15 min. Cells were lysed in M-PER (Mammalian protein extraction reagent, Thermo Fisher) buffer with protease inhibitors; cell lysates were then subjected to analytical ultracentrifugation.

Glycerol gradient ultracentrifugation combined with the rapid and accurate micro-fractionation of the contents of a small centrifuge tube was conducted by following a procedure adapted from the post-centrifugation micro-fractionation method of Darawshe, Rivas, and Minton⁴⁸. A 15–45% glycerol gradient containing M-PER lysis buffer was constructed by layering solutions at decreasing percentages of 45–15% glycerol on top of each other (13 layers, 98 μl each, total volume 1.20 ml; height 3.0 cm) in an 11 \times 34 mm centrifuge tube. A 50- μl sample solution was layered on top of the gradient, followed by 50 μl of silicon oil to prevent evaporation. The tubes were then placed in a pre-cooled bucket and centrifuged for 5 h at a rotor speed of 55,000 rpm at 4 °C in an Optima TLX preparative ultracentrifuge using a swinging bucket TLS-55 rotor (Beckman Coulter, Indianapolis, IN). Post-deceleration was performed without breaking, and the tube was immediately placed on ice. Micro-fractionation of the tube contents was completed by using a BRANDEL automated micro-fractionator equipped with an FR-HA 1.0 block assembly (Brandel, Gaithersburg, MD). The tube was placed in the receptacle, and fractions were removed from the upper surface of the solution by stepwise elevation of the receptacle by a precise increment of height. A total of 27 fractions were collected in a 96-well plate, with each fraction being ~45 μl in volume except the bottom fraction (fraction 27), which was 125 μl . The fractions were analyzed by western blotting.

Membrane thermal shift assays

Membrane thermal shift assays were performed as described previously³². Human ABCC4-expressing membrane vesicles from HEK293 cells (Solvo Biotechnology, Hungary, Cat. #SBVT07) were purchased from Sigma-Aldrich (St. Louis, MO). To assess the ability of ligands to thermally stabilize ABCC4, membrane vesicles (5 μg protein/20 μl final reaction volume) in 1 \times assay buffer (SB PREDIVEZ™ Reagent Kit, Cat. #SBPVR4, Solvo Biotechnology, Hungary) were incubated with ligand (20 μM Cee2 or 5 mM MgATP) for 60 min at 37 °C. Samples were then heated in a thermocycler for 3 min at various temperatures (37–68 °C) to calculate the melting temperature (T_m). Samples were treated with ice-cold PBS supplemented with NP-40 to a final concentration of 0.8%. Subsequently, ultracentrifugation (at 100,000 $\times g$ for 20 min at 4 °C) was performed to precipitate the denatured proteins. The supernatant was subjected to immunoblot analysis using an ABCC4 antibody. The signal intensity at various temperatures was normalized to that at 37 °C. Based on an extrapolation from the thermal denaturation curve that produced 99% loss of protein in the supernatant, 60 °C was selected for the isothermal shift assay. To assess the effect of Cee2 on MgATP-ABCC4 interactions, membranes were preincubated with 20 μM Cee2 for 60 min at 37 °C. After the incubation, 5 mM MgATP was added and incubated for an additional 60 min at 37 °C. Samples were then heated for 3 min at 60 °C.

Pathway analysis

Pathway analysis of the significantly different proteins was performed using the Enrichr database. The pathway enrichment was determined based on the p-value that ranked the output pathways by abundance in the gene lists.

Statistical analysis and data visualization

Statistical analysis was performed by using GraphPad Prism 10. The significance of the difference was determined by using Student's *t*-test or one-way ANOVA, where applicable. *P*-values of <0.05 were considered to be significant. The protein network of prey proteins identified from Avi- and APEX-affinity purification MS experiments was obtained from the STRING database version 11.5, and data visualization of the network was done by using Cytoscape version 3.7.2.

Reporting summary

Further information on research design is available in the Nature Portfolio Reporting Summary linked to this article.

Data availability

Data generated in this study are provided in the Supplementary Information/Source Data file. The mass spectrometry raw data in this study have been deposited in the ProteomeXchange database under accession code PXD048010 [<http://proteomecentral.proteomexchange.org/cgi/GetDataset?ID=PX048010>]. The authors declare no competing interests. Source data are provided with this paper.

References

1. Indolfi, C. et al. Activation of cAMP-PKA signaling in vivo inhibits smooth muscle cell proliferation induced by vascular injury. *Nat. Med.* **3**, 775–779 (1997).
2. Houslay, M. D. Underpinning compartmentalised cAMP signalling through targeted cAMP breakdown. *Trends Biochem. Sci.* **35**, 91–100 (2010).
3. Buxton, I. L. & Brunton, L. L. Compartments of cyclic AMP and protein kinase in mammalian cardiomyocytes. *J. Biol. Chem.* **258**, 10233–10239 (1983).
4. Zaccolo, M. & Pozzan, T. Discrete microdomains with high concentration of cAMP in stimulated rat neonatal cardiac myocytes. *Science* **295**, 1711–1715 (2002).

5. Ponsioen, B. et al. Detecting cAMP-induced Epac activation by fluorescence resonance energy transfer: Epac as a novel cAMP indicator. *EMBO Rep.* **5**, 1176–1180 (2004).
6. Wijaya, J. et al. An ABC transporter drives medulloblastoma pathogenesis by regulating Sonic Hedgehog signaling. *Cancer Res.* **80**, 1524–1537 (2020).
7. Sinha, C. et al. PKA and actin play critical roles as downstream effectors in MRP4-mediated regulation of fibroblast migration. *Cell. Signal.* **27**, 1345–1355 (2015).
8. Sinha, C. et al. Multi-drug resistance protein 4 (MRP4)-mediated regulation of fibroblast cell migration reflects a dichotomous role of intracellular cyclic nucleotides. *J. Biol. Chem.* **288**, 3786–3794 (2013).
9. Zhang, G., Liu, Y., Ruoho, A. E. & Hurley, J. H. Structure of the adenyllyl cyclase catalytic core. *Nature* **386**, 247–253 (1997).
10. van Aubel, R., Smeets, P. H. E., Peters, J. G. P., Bindels, R. J. M. & Russel, F. G. M. The MRP4/ABCC4 gene encodes a novel apical organic anion transporter in human kidney proximal tubules: putative efflux pump for urinary cAMP and cGMP. *J. Am. Soc. Nephrol.* **13**, 595–603 (2002).
11. Sager, G. & Ravna, A. W. Cellular efflux of cAMP and cGMP - a question about selectivity. *Mini Rev. Med. Chem.* **9**, 1009–1013 (2009).
12. Arora, K. et al. Compartmentalization of cyclic nucleotide signaling: a question of when, where, and why?. *Pflug. Arch.* **465**, 1397–1407 (2013).
13. Belleville-Rolland, T. et al. Role of membrane lipid rafts in MRP4 (ABCC4) dependent regulation of the cAMP pathway in blood platelets. *Thromb. Haemost.* **121**, 1628–1636 (2021).
14. Sassi, Y. et al. Multidrug resistance-associated protein 4 regulates cAMP-dependent signaling pathways and controls human and rat SMC proliferation. *J. Clin. Investig.* **118**, 2747–2757 (2008).
15. Depry, C., Allen, M. D. & Zhang, J. Visualization of PKA activity in plasma membrane microdomains. *Mol. Biosyst.* **7**, 52–58 (2011).
16. Li, C. et al. Spatiotemporal coupling of cAMP transporter to CFTR chloride channel function in the gut epithelia. *Cell* **131**, 940–951 (2007).
17. Tomes, C., Rossi, S. & Moreno, S. Isobutylmethylxanthine and other classical cyclic nucleotide phosphodiesterase inhibitors affect cAMP-dependent protein kinase activity. *Cell. Signal.* **5**, 615–621 (1993).
18. Seamon, K. B., Padgett, W. & Daly, J. W. Forskolin: unique diterpene activator of adenylate cyclase in membranes and in intact cells. *Proc. Natl. Acad. Sci. USA* **78**, 3363–3367 (1981).
19. Cheung, L. et al. High-throughput screening identifies Ceefourin 1 and Ceefourin 2 as highly selective inhibitors of multidrug resistance protein 4 (MRP4). *Biochem. Pharm.* **91**, 97–108 (2014).
20. Adderley, S. P. et al. Iloprost- and isoproterenol-induced increases in cAMP are regulated by different phosphodiesterases in erythrocytes of both rabbits and humans. *Am. J. Physiol. Heart Circ. Physiol.* **296**, H1617–H1624 (2009).
21. Li, Y. & Sousa, R. Expression and purification of E. coli BirA biotin ligase for in vitro biotinylation. *Protein Expr. Purif.* **82**, 162–167 (2012).
22. Lomant, A. J. & Fairbanks, G. Chemical probes of extended biological structures: synthesis and properties of the cleavable protein cross-linking reagent [35S]dithiobis(succinimidyl propionate). *J. Mol. Biol.* **104**, 243–261 (1976).
23. Choi, H. et al. SAINT: probabilistic scoring of affinity purification-mass spectrometry data. *Nat. Methods* **8**, 70–U100 (2011).
24. Jayasena, T. et al. Application of targeted mass spectrometry for the quantification of sirtuins in the central nervous system. *Sci. Rep.* **6**, 35391 (2016).
25. Ranjit, S. et al. ABCC4 impacts megakaryopoiesis and protects megakaryocytes against 6-mercaptopurine induced cytotoxicity. *Drug Resist. Updat.* **72**, 101017 (2024).
26. Pitre, A. et al. An unexpected protein interaction promotes drug resistance in leukemia. *Nat. Commun.* **8**, 1547 (2017).
27. Dumrongprechachan, V. et al. Cell-type and subcellular compartment-specific APEX2 proximity labeling reveals activity-dependent nuclear proteome dynamics in the striatum. *Nat. Commun.* **12**, 4855 (2021).
28. Sabo, J. et al. CKAP5 enables formation of persistent actin bundles templated by dynamically instable microtubules. *Curr. Biol.* **34**, 260–272 e267 (2024).
29. Inoue, S. et al. Drebrin-like (Dbn1) controls neuronal migration via regulating N-cadherin expression in the developing cerebral cortex. *J. Neurosci.* **39**, 678–691 (2019).
30. Cueille, N. et al. Characterization of MAP1B heavy chain interaction with actin. *Brain Res. Bull.* **71**, 610–618 (2007).
31. Gose, T. et al. ABCG2 requires a single aromatic amino acid to “clamp” substrates and inhibitors into the binding pocket. *FASEB J.* **34**, 4890–4903 (2020).
32. Gose, T. et al. The net electrostatic potential and hydration of ABCG2 affect substrate transport. *Nat. Commun.* **14**, 5035 (2023).
33. Dvorak, V. et al. An overview of cell-based assay platforms for the solute carrier family of transporters. *Front. Pharm.* **12**, 722889 (2021).
34. Huang, Y. et al. Structural basis for substrate and inhibitor recognition of human multidrug transporter MRP4. *Commun. Biol.* **6**, 549 (2023).
35. Lusvarghi, S. & Ambudkar, S. V. ATP-dependent thermostabilization of human P-glycoprotein (ABCB1) is blocked by modulators. *Biochem. J.* **476**, 3737–3750 (2019).
36. Chytla, A. et al. Not just another scaffolding protein family: the multifaceted MPPs. *Molecules* **25**, <https://doi.org/10.3390/molecules25214954> (2020).
37. Hayashi, H. et al. Sorting nexin 27 interacts with multidrug resistance-associated protein 4 (MRP4) and mediates internalization of MRP4. *J. Biol. Chem.* **287**, 15054–15065 (2012).
38. Xu, P., Duong, D. M. & Peng, J. Systematical optimization of reverse-phase chromatography for shotgun proteomics. *J. Proteome Res.* **8**, 3944–3950 (2009).
39. Wang, X. et al. JUMP: a tag-based database search tool for peptide identification with high sensitivity and accuracy. *Mol. Cell. Proteom.* **13**, 3663–3673 (2014).
40. Elias, J. E. & Gygi, S. P. Target-decoy search strategy for increased confidence in large-scale protein identifications by mass spectrometry. *Nat. Methods* **4**, 207–214 (2007).
41. Zhou, J. Y. et al. Galectin-3 is a candidate biomarker for amyotrophic lateral sclerosis: discovery by a proteomics approach. *J. Proteome Res.* **9**, 5133–5141 (2010).
42. Deutsch, E. W. et al. The ProteomeXchange consortium at 10 years: 2023 update. *Nucleic Acids Res.* **51**, D1539–D1548 (2023).
43. Perez-Riverol, Y. et al. The PRIDE database resources in 2022: a hub for mass spectrometry-based proteomics evidences. *Nucleic Acids Res.* **50**, D543–D552 (2022).
44. Perez-Riverol, Y. et al. PRIDE Inspector Toolsuite: moving toward a universal visualization tool for proteomics data standard formats and quality assessment of ProteomeXchange datasets. *Mol. Cell. Proteom.* **15**, 305–317 (2016).
45. Marciano, R., Leprivier, G. & Rotblat, B. Puromycin labeling does not allow protein synthesis to be measured in energy-starved cells. *Cell Death Dis.* **9**, 39 (2018).
46. Graham, J. M. Fractionation of Golgi, endoplasmic reticulum, and plasma membrane from cultured cells in a preformed continuous iodixanol gradient. *Sci. World J.* **2**, 1435–1439 (2002).
47. Graham, J., Ford, T. & Rickwood, D. The preparation of subcellular organelles from mouse liver in self-generated gradients of iodixanol. *Anal. Biochem.* **220**, 367–373 (1994).

48. Darawshe, S., Rivas, G. & Minton, A. P. Rapid and accurate microfractionation of the contents of small centrifuge tubes: application in the measurement of molecular weight of proteins via sedimentation equilibrium. *Anal. Biochem.* **209**, 130–135 (1993).

Acknowledgements

We thank St. Jude Children's Research Hospital's Department of Structural Biology, Center for Proteomics and Metabolomics, and Cell and Tissue Imaging Center for their respective assistance with glycerol gradient ultracentrifugation, proteomic studies, and confocal and TIRF imaging. This work was supported by National Institutes of Health (NIH) grants R01 CA194057, CA194206, P30 CA21745, CA21865, 5R01DK080834, NCI P30 CA021765, CA96832, and ALSAC.

Author contributions

J.Z., S.R., T.G., J.L., A.N., V.R.P., Y.W., A.P., and R.C. performed experiments; J.Z., S.R., T.G., Z.-F.Y., A.N., V.R.P., A.P., R.C., and J.D.S. analyzed and interpreted data; J.D.S. and J.P. supervised the research; J.W. and A.P.N. provided editorial and intellectual input; S.R., J.Z., and J.D.S. drafted the manuscript; all authors critically reviewed and approved the manuscript.

Competing interests

The authors declare no competing interests.

Additional information

Supplementary information The online version contains supplementary material available at <https://doi.org/10.1038/s41467-025-66877-4>.

Correspondence and requests for materials should be addressed to John D. Schuetz.

Peer review information *Nature Communications* thanks Markku Varjosalo and the other, anonymous, reviewer(s) for their contribution to the peer review of this work. A peer review file is available.

Reprints and permissions information is available at <http://www.nature.com/reprints>

Publisher's note Springer Nature remains neutral with regard to jurisdictional claims in published maps and institutional affiliations.

Open Access This article is licensed under a Creative Commons Attribution-NonCommercial-NoDerivatives 4.0 International License, which permits any non-commercial use, sharing, distribution and reproduction in any medium or format, as long as you give appropriate credit to the original author(s) and the source, provide a link to the Creative Commons licence, and indicate if you modified the licensed material. You do not have permission under this licence to share adapted material derived from this article or parts of it. The images or other third party material in this article are included in the article's Creative Commons licence, unless indicated otherwise in a credit line to the material. If material is not included in the article's Creative Commons licence and your intended use is not permitted by statutory regulation or exceeds the permitted use, you will need to obtain permission directly from the copyright holder. To view a copy of this licence, visit <http://creativecommons.org/licenses/by-nc-nd/4.0/>.

© The Author(s) 2025